

# Rossby wave instability in weakly ionized protoplanetary disks. II. radial B-fields

Can Cui<sup>1,2\*</sup> and Zijin Wang<sup>3</sup>

<sup>1</sup>*Department of Astronomy and Astrophysics, University of Toronto, Toronto, ON M5S 3H4, Canada*

<sup>2</sup>*DAMTP, University of Cambridge, Wilberforce Road, Cambridge CB3 0WA, UK*

<sup>3</sup>*Department of Mathematics, University of Toronto, Toronto, ON M5S 2E4, Canada*

6 August 2024

## ABSTRACT

Building on our first paper in this series, we investigate the impact of radial magnetic fields and non-ideal magnetohydrodynamic (MHD) effects — specifically, Ohmic resistivity, Hall drift, and ambipolar diffusion — on RWI unstable modes. The presence of a radial field is linked to the disk’s vertical shear and vertical magnetic field. We perform radially global linear analyses and utilize the spectral code DEDALUS to solve the matrix eigenvalue problems. Our findings reveal that radial fields exhibit behavior similar to vertical fields. In the ideal MHD limit, radial fields enhance the effect of vertical fields in reducing growth rates, with significant reductions starting at relatively weak field strengths, around  $\beta \sim 10^3 - 10^4$ , which are relevant to protoplanetary disks. In the non-ideal MHD limit, all three non-ideal effects, when sufficiently strong, cause the growth rates to closely resemble those observed in hydrodynamic models.

**Key words:** instabilities – MHD – methods: analytical – protoplanetary disks

## 1 INTRODUCTION

The evolution of dust particles in protoplanetary disks is a complex process. Micron-sized dust grains grow into kilometer-sized planetesimals, ultimately forming terrestrial planets or the cores of gas giants (Armitage 2011). This growth, however, is hindered by several barriers such as bouncing, fragmentation, and rapid radial drift (Weidenschilling 1977; Güttler et al. 2010; Zsom et al. 2010). To overcome these challenges, the Rossby wave instability (RWI) perhaps present a promising mechanism. RWI could generate large, lopsided crescent-shaped vortices that concentrate dust grains towards pressure maxima, thereby promoting streaming instability and gravitational collapse (Goldreich & Ward 1973; Weidenschilling & Cuzzi 1993; Youdin & Goodman 2005). These vortices may be responsible for the azimuthal asymmetries observed in (sub-)millimeter dust continuum and CO rotational transition lines by ALMA (Huang et al. 2018; van der Marel et al. 2021).

The necessary RWI condition is local extrema in the radial vortensity profile,  $(\Sigma\Omega/\kappa^2)S^{2/\Gamma}$  (Lovelace et al. 1999; Li et al. 2000; Chang et al. 2023; Chang & Youdin 2024). It gives rise to the exponential growth of non-axisymmetric modes ( $\propto \exp[i m \phi]$ , where  $m = 1, 2, \dots$ ) on each side of the

corotation radius (Tsang & Lai 2008). These unstable Rossby modes are confined between the inner and outer Lindblad resonances, where density waves are launched (Lin & Shu 1964; Goldreich & Tremaine 1979). In the context of protoplanetary disks, RWI numerical simulations have commonly been performed in the scene of gap edges carved by a planet (Zhu et al. 2014; Zhu & Stone 2014; Hammer et al. 2017; Li et al. 2020; Cimerman & Rafikov 2023), dead zone edges of the magneto-rotational instability (MRI; Lyra & Mac Low 2012; Miranda et al. 2016, 2017), and magnetically induced rings and gaps (Hsu et al. 2024), where local vortensity extrema can occur. These simulations elucidate that the non-linear saturation of the Rossby vortices is primarily governed by  $m = 1$  modes (Godon & Livio 1999; Li et al. 2001; Meheut et al. 2012).

Protoplanetary disks are likely magnetized, with magnetic fields originating from primordial molecular clouds (Galli & Shu 1993; Girart et al. 2006, 2009). Magnetic fields are believed to be a key factor of disk accretion and evolution, mainly through the magnetized disk winds, MRI turbulence, and laminar magnetic stress. Furthermore, owing to weak thermal and non-thermal ionization, the gas and magnetic fields are only poorly coupled, rendering the disk weakly ionized. Consequently, the gas dynamics bears on three non-ideal magnetohydrodynamic (MHD) effects – Ohmic resistivity, Hall drift, and ambipolar diffusion (Lesur 2021). Therefore, it would be of significance to study RWI modes in the

\* [can.cui@astro.utoronto.ca](mailto:can.cui@astro.utoronto.ca)

presence of magnetism. In [Paper I](#), we investigate the RWI modes for constant azimuthal or vertical fields. Generically the growth rates are diminished with strong fields in the ideal regime, but are revived by non-ideal MHD effects. In this work, we extend our exploration to radial magnetic fields, which arise when disk vertical shear and vertical fields are present.

This paper is organized as follows. In [Section 2](#), we introduce the governing dynamical equations, equilibrium state, and perturbation equations that delineate our theoretical framework. [Section 3](#) elaborates on the numerical methodologies employed to solve the set of ordinary differential equations (ODEs) governing the magnetized RWI. In [Section 4](#), we present numerical solutions obtained and elucidate the RWI modes behaviors. Lastly, we summarize the main findings in [Section 5](#).

## 2 THEORY

### 2.1 Dynamical equations

The stability of a three-dimensional, compressible, magnetized disk with background radial vortensity extrema is investigated using cylindrical coordinates  $(r, \phi, z)$ . The gravitational potential is given by  $\Phi = -GM/(r^2 + z^2)^{1/2}$ , where  $M$  is the mass of the central star. Disk self-gravity is neglected. The governing equations for this magnetized disk, expressed in Gaussian units, include the continuity equation, momentum conservation, entropy conservation, and the induction equation,

$$\frac{d\rho}{dt} + \rho \nabla \cdot \mathbf{v} = 0, \quad (1)$$

$$\frac{d\mathbf{v}}{dt} + \frac{1}{\rho} \nabla \left[ P + \frac{B^2}{8\pi} \right] + \nabla \Phi - \frac{1}{4\pi\rho} (\mathbf{B} \cdot \nabla) \mathbf{B} = 0, \quad (2)$$

$$\frac{dS}{dt} = 0, \quad (3)$$

$$\frac{\partial \mathbf{B}}{\partial t} - \nabla \times (\mathbf{v} \times \mathbf{B} - c\mathbf{E}') = 0. \quad (4)$$

The material derivative is defined as  $d/dt \equiv \partial/\partial t + \mathbf{v} \cdot \nabla$ , and  $S \equiv P/\rho^\Gamma$  denotes the entropy of disk matter.

The non-ideal MHD terms manifest in the electric field of the rest fluid frame,

$$\mathbf{E}' = \frac{4\pi}{c^2} [\eta_O \mathbf{J} + \eta_H \mathbf{J} \times \mathbf{b} - \eta_A (\mathbf{J} \times \mathbf{b}) \times \mathbf{b}], \quad (5)$$

where the unit vector of magnetic field is denoted by  $\mathbf{b} = \mathbf{B}/|B|$ , and the current density is  $\mathbf{J} = c\nabla \times \mathbf{B}/4\pi$ . The diffusivities are  $\eta_O$ ,  $\eta_H$ , and  $\eta_A$  for Ohmic, Hall, and ambipolar diffusion, respectively, and are expressed by ([Wang et al. 2019](#); [Lesur 2021](#))

$$\eta_O = \frac{c^2}{4\pi} \left( \frac{1}{\sigma_O} \right), \quad (6)$$

$$\eta_H = \frac{c^2}{4\pi} \left( \frac{\sigma_H}{\sigma_H^2 + \sigma_P^2} \right), \quad (7)$$

$$\eta_A = \frac{c^2}{4\pi} \left( \frac{\sigma_P}{\sigma_H^2 + \sigma_P^2} \right) - \eta_O, \quad (8)$$

where  $\sigma_O$ ,  $\sigma_H$  and  $\sigma_P$  are Ohmic, Hall, and Pederson conductivities. For  $j^{\text{th}}$  charged species, let  $Z_j e$  be the charge and  $n_j$  the number density, then

$$\sigma_O = \frac{ec}{B} \sum_j n_j Z_j \beta_j, \quad (9)$$

$$\sigma_H = \frac{ec}{B} \sum_j \frac{n_j Z_j}{1 + \beta_j^2}, \quad (10)$$

$$\sigma_P = \frac{ec}{B} \sum_j \frac{n_j Z_j \beta_j}{1 + \beta_j^2}, \quad (11)$$

in which  $\beta_j$  is the Hall parameter defined as the ratio of the gyrofrequency to the collision rate with neutrals ([Wardle & Ng 1999](#)),

$$\beta_j = \frac{Z_j e B}{m_j c} \frac{1}{\gamma_j \rho}, \quad (12)$$

and

$$\gamma_j = \frac{\langle \sigma v \rangle_j}{m_n + m_j}, \quad (13)$$

where  $m_j$  is the molecular mass of charged species,  $m_n$  is the mean molecular mass of the neutrals, and  $\langle \sigma v \rangle_j$  is the momentum exchange rate between the  $j^{\text{th}}$  species and the neutrals.

Finally, we introduce the dimensionless Elsässer numbers that quantify the strengths of non-ideal MHD effects,

$$\Lambda = \frac{v_A^2}{\eta_O \Omega_K}, \quad \text{Ha} = \frac{v_A^2}{\eta_H \Omega_K}, \quad \text{Am} = \frac{v_A^2}{\eta_A \Omega_K}, \quad (14)$$

where the Alfvén velocity is  $v_A^2 = B^2/4\pi\rho$ , and  $\Omega_K$  is the Keplerian angular speed. The Elsässer numbers are inverse proportional to diffusivities. Also note that  $\Lambda$  and  $\text{Ha}$  are  $B$ -dependent, as  $\eta_O \propto \text{const}$ ,  $\eta_H \propto B$ ,  $\eta_A \propto B^2$ .

### 2.2 Equilibrium solutions

The equilibrium disk model is stationary ( $\partial/\partial t = 0$ ), axisymmetric ( $\partial/\partial\phi = 0$ ), and radially global. All background quantities are independent of  $z$ . The presence of radial field requires  $z \neq 0$ , where the vertical shear vanishes ([Barker & Latter 2015](#)). The steady-state physical quantities are denoted by the subscript “0”. The equilibrium velocity field has only the azimuthal component  $\mathbf{v}_0 = (0, v_{\phi 0}, 0)$ .

To establish vortensity extrema, we follow [Paper I](#) by introducing a Gaussian bump centered at  $r = r_0$  in the density profile,

$$\frac{\rho_0}{\rho_{00}} = 1 + (A - 1) \exp \left[ -\frac{1}{2} \left( \frac{r - r_0}{\Delta r} \right)^2 \right], \quad (15)$$

where  $\rho_{00}$  represents the background density profile without the Gaussian bump and is assumed to be constant for simplicity. A barotropic flow is adopted, with the pressure related to density by

$$\frac{P_0}{P_{0*}} = \left[ \frac{\rho_0}{\rho_{0*}} \right]^\Gamma, \quad (16)$$

where subscript “0\*” denotes background quantities evaluated at  $r_0$ , and  $\Gamma$  is the adiabatic index. The adiabatic sound speed is defined as  $c_{s0} \equiv (\Gamma P_0/\rho_0)^{1/2}$ . By specifying the disk aspect ratio to be  $c_{s0^*}/v_{K0^*} = 0.06$ , we can obtain  $P_{0^*}$  and subsequently  $P_0$ . We follow [Paper I](#) and set  $GM = \rho_0 = r_0 = 1$ ,  $\Delta r/r_0 = 0.05$ ,  $\Gamma = 5/3$ ,  $A = 1.5$ . In equilibrium, with constant background magnetic fields, the radial momentum equation is given by

$$\frac{v_{\phi 0}^2}{r} = \frac{1}{\rho_0} \frac{\partial P_0}{\partial r} + \frac{\partial \Phi}{\partial r}. \quad (17)$$

Owing to the complexity of achieving magnetic equilibrium in cylindrical coordinates, we adopt the solution from [Latter & Papaloizou \(2018\)](#), where a magnetic steady state is established in a local shearing box model. The magnetic field vector  $\mathbf{B}_0 = (B_{r0}, 0, B_{z0})$  is set to a constant. The unit vector of the background field is then  $\mathbf{b}_0 = (b_{r0}, 0, b_{z0}) = (B_{r0}/|B|, 0, B_{z0}/|B|)$ . We omit curvature terms in  $\nabla \cdot \mathbf{B}$ , such that the divergence free condition is satisfied. In a local disk, the components of the magnetic field must satisfy  $\mathbf{B}_0 \cdot \nabla \mathbf{v}_0 = 0$ , which implies

$$\frac{B_{r0}}{B_{z0}} = -\frac{q_z}{q_r}, \quad (18)$$

where

$$q_r \equiv -\frac{\partial \ln \Omega}{\partial \ln r}, \quad (19)$$

$$q_z \equiv -\frac{r \partial \ln \Omega}{\partial z}. \quad (20)$$

Eq. (18) is equivalent to eq. (10) in [Cui et al. \(2024\)](#) after eliminating the curvature terms. The dimensionless radial shear is parameterized by  $q_r$ , for which  $q_r = 3/2$  for a Keplerian disk. The presence of  $B_{r0}$  is linked to disk’s vertical shear, parameterized by the dimensionless quantity  $q_z$ . Unlike  $q_r$ , which is generally positive for protoplanetary disks, the sign of  $q_z$  reverses with respect to the midplane ([Barker & Latter 2015](#)). Above the midplane ( $z > 0$ ),  $q_z > 0$ , and below the midplane ( $z < 0$ ),  $q_z < 0$ . In protoplanetary disks,  $|q_z| \sim h$ , leading to  $|B_{r0}/B_{z0}| \ll 1$ . In magnetic equilibrium, we set  $q_r = 3/2$  and  $|q_z| = h$  for simplicity. When seeking numerical solutions, we set  $B_{z0}$  to a constant, and  $B_{z0} > 0$  without loss of generality. The strength of  $B_{z0}$  is parameterized by the vertical plasma  $\beta$ , defined as the ratio of gas pressure to vertical magnetic pressure,  $\beta = 8\pi P_0/B_{z0}^2$ . Given constant background fields, equilibrium in the non-ideal limit is achieved.

### 2.2.1 Solberg-Hoiland criterion

The stability of the equilibrium disk, including the Gaussian bump, against axisymmetric adiabatic perturbations shall be examined. For hydrodynamic fluids, the general condition for stability is given by the Solberg-Hoiland criterion, where the stability is ensured if ([Tassoul 1978](#))

$$\kappa^2 + N^2 \geq 0, \quad (21)$$

where the epicyclic frequency is defined as  $\kappa = [r^{-3} d(r^4 \Omega^2)/dr]^{1/2}$ , and  $N$  is the buoyancy frequency,

$$N^2 = N_r^2 + N_z^2, \quad (22)$$

in which

$$N_r^2 = -\frac{1}{\Gamma \rho} \frac{\partial P}{\partial r} \frac{\partial \ln S}{\partial r}, \quad N_z^2 = -\frac{1}{\Gamma \rho} \frac{\partial P}{\partial z} \frac{\partial \ln S}{\partial z}. \quad (23)$$

For a barotropic flow,  $N^2$  is zero, and the condition  $\kappa^2 \geq 0$  is satisfied for the set of parameters chosen in this work.

### 2.3 Perturbation equations

Consider small perturbations to eqs. (1)-(4), such that physical quantities are composed of a background state and a perturbation part, for example,  $\mathbf{B} = \mathbf{B}_0 + \delta \mathbf{B}(r, z, \phi, t)$ . We consider Eulerian perturbations of the form  $\propto f(r) \exp(ik_z z + im\phi - i\omega t)$ , where  $k_z$  is the vertical wavenumber,  $m$  is the azimuthal mode number, and  $\omega = \omega_r + i\gamma$  is the mode frequency, with  $\gamma$  denoting the growth rate. We further define the Doppler-shifted wave frequency  $\Delta\omega = \omega - m\Omega$ , the azimuthal wavenumber  $k_\phi = m/r$ .

We now drop subscript “0” for background quantities throughout rest of the paper. Our model encompasses eight perturbed quantities:  $\delta \mathbf{v}$ ,  $\delta \mathbf{B}$ ,  $\delta \rho$ ,  $\delta \Psi$ . The perturbed enthalpy is

$$\delta \Psi = \frac{\delta P}{\rho}, \quad (24)$$

and

$$\frac{\partial \delta \Psi}{\partial r} = \frac{1}{\rho} \frac{\partial \delta P}{\partial r} - \frac{1}{\rho} \frac{\partial \rho}{\partial r} \delta \Psi. \quad (25)$$

Furthermore, the length scales of entropy, pressure, and density variations are defined as

$$L_S \equiv \frac{\Gamma}{d \ln S/dr}, \quad L_P \equiv \frac{\Gamma}{d \ln P/dr}, \quad L_\rho \equiv \frac{1}{d \ln \rho/dr}. \quad (26)$$

These length scales are related by

$$\frac{1}{L_P} = \frac{1}{L_S} + \frac{1}{L_\rho}. \quad (27)$$

For a barotropic flow, the length scale of entropy approaches infinity,  $1/L_S \rightarrow 0$ .

It follows that the perturbed continuity and entropy equations read

$$\frac{\partial \delta v_r}{\partial r} + \left[ \frac{1}{r} + \frac{1}{L_\rho} \right] \delta v_r + ik_\phi \delta v_\phi - i\Delta\omega \frac{\delta \Psi}{c_s^2} = 0, \quad (28)$$

$$\delta \Psi = c_s^2 \frac{\delta \rho}{\rho}. \quad (29)$$

The linearized momentum and induction equations are presented as follows.

#### 2.3.1 ideal MHD regime

The three-components of momentum equation are

$$-i\Delta\omega \delta v_r - 2\Omega \delta v_\phi + \frac{\partial \delta \Psi}{\partial r} + \frac{B_z}{4\pi \rho} \left[ \frac{\partial \delta B_z}{\partial r} - ik_z \delta B_r \right] = 0, \quad (30)$$

$$\begin{aligned}
& -i\Delta\omega\delta v_\phi + \frac{\kappa^2}{2\Omega}\delta v_r + ik_\phi\delta\Psi \\
& + \frac{1}{4\pi\rho}\left[ ik_\phi(B_r\delta B_r + B_z\delta B_z) - B_r\left(\frac{\partial\delta B_\phi}{\partial r} + \frac{\delta B_\phi}{r}\right) \right. \\
& \quad \left. - ik_z B_z\delta B_\phi \right] = 0, \tag{31}
\end{aligned}$$

$$-i\Delta\omega\delta v_z + ik_z\delta\Psi + \frac{B_r}{4\pi\rho}\left[ ik_z\delta B_r - \frac{\partial\delta B_z}{\partial r} \right] = 0, \tag{32}$$

and the three-components of induction equation in the ideal limit are

$$-i\Delta\omega\delta B_r - ik_z B_z\delta v_r + \left[ \frac{\delta v_r}{r} + ik_\phi\delta v_\phi + ik_z\delta v_z \right] B_r + C_1 = 0, \tag{33}$$

$$-i\Delta\omega\delta B_\phi + \left[ \frac{\delta v_\phi}{r} - \frac{\partial\delta v_\phi}{\partial r} \right] B_r + \left[ \frac{v_\phi}{r} - \frac{\partial v_\phi}{\partial r} \right] \delta B_r - ik_z B_z\delta v_\phi + C_2 = 0, \tag{34}$$

$$-i\Delta\omega\delta B_z - \frac{\partial\delta v_z}{\partial r} B_r + \left[ \frac{\partial\delta v_r}{\partial r} + \frac{\delta v_r}{r} + ik_\phi\delta v_\phi \right] B_z + C_3 = 0, \tag{35}$$

where  $C_1, C_2, C_3$  present non-ideal MHD terms that will be presented in the next subsection.

### 2.3.2 non-ideal MHD regime

We now derive the perturbation equations for non-ideal MHD effects, omitting the curvature terms in  $C_1, C_2$ , and  $C_3$  for simplicity. As shown in Appendix A, curvature terms only slightly affect the growth rates. Compared to the pure  $B_z$  model in Paper I, Ohmic resistivity involves the same non-ideal MHD terms. However, the other two non-ideal terms include additional components due to the presence of a radial field. The three components of the induction equations are

$$\begin{aligned}
C_1 = & -\eta_O \left[ \frac{\partial^2\delta B_r}{\partial r^2} - (k_\phi^2 + k_z^2)\delta B_r \right] \\
& + \eta_H \left[ ib_z k_z + b_r \frac{\partial}{\partial r} \right] [ik_\phi\delta B_z - ik_z\delta B_\phi] \\
& - \eta_A \left[ \left( -b_z^2 k_z^2 + b_r^2 \frac{\partial^2}{\partial r^2} + 2b_r b_z ik_z \frac{\partial}{\partial r} \right) \delta B_r \right. \\
& \quad \left. + \left( \frac{\partial^2}{\partial r^2} - k_\phi^2 - k_z^2 \right) (\delta B_r b_r + \delta B_z b_z) b_r \right] \tag{36}
\end{aligned}$$

$$\begin{aligned}
C_2 = & -\eta_O \left[ \frac{\partial^2\delta B_\phi}{\partial r^2} - (k_\phi^2 + k_z^2)\delta B_\phi \right] \\
& + \eta_H \left[ ib_z k_z + b_r \frac{\partial}{\partial r} \right] \left[ ik_z\delta B_r - \frac{\partial\delta B_z}{\partial r} \right] \\
& - \eta_A \left[ -b_z^2 k_z^2 + b_r^2 \frac{\partial^2}{\partial r^2} + 2b_r b_z ik_z \frac{\partial}{\partial r} \right] \delta B_\phi \tag{37}
\end{aligned}$$

$$\begin{aligned}
C_3 = & -\eta_O \left[ \frac{\partial^2\delta B_z}{\partial r^2} - (k_\phi^2 + k_z^2)\delta B_z \right] \\
& + \eta_H \left[ ib_z k_z + b_r \frac{\partial}{\partial r} \right] \left[ \frac{\partial\delta B_\phi}{\partial r} - ik_\phi\delta B_r \right] \\
& - \eta_A \left[ \left( -b_z^2 k_z^2 + b_r^2 \frac{\partial^2}{\partial r^2} + 2b_r b_z ik_z \frac{\partial}{\partial r} \right) \delta B_z \right. \\
& \quad \left. + \left( \frac{\partial^2}{\partial r^2} - k_\phi^2 - k_z^2 \right) (\delta B_r b_r + \delta B_z b_z) b_z \right] \tag{38}
\end{aligned}$$

## 3 NUMERICAL METHODS

We solve the linearized equations presented in §2.3 numerically using pseudospectral methods as described in Paper I. Solutions of differential equations are approximated at selected collocation points by a weighted sum of orthogonal basis functions. Chebyshev polynomials of the first kind,  $T_n$ , where  $n = 0, 1, 2, \dots, N-1$ , are used as the basis. The radial domain, spanning  $r \in [0.4, 1.6]$ , is discretized into  $N$  Chebyshev collocation points. To minimize interpolation errors, these nodes are non-uniform and are computed as the roots of the  $N$ th-degree Chebyshev polynomial,  $T_N$ .

The differential equations described in §2.3 form standard linear eigenvalue problems, which can be expressed compactly in a generalized matrix form:

$$A\vec{x} = \mathcal{L}\vec{x} + \omega\mathcal{M}\vec{x} = 0, \tag{39}$$

where  $\omega$  represents the eigenvalue,  $\vec{x} = [\delta v_r, \delta B_r, \delta v_\phi, \dots]^T$  is a vector of eigenfunctions containing  $M$  perturbed quantities, and  $A, \mathcal{L}$ , and  $\mathcal{M}$  are  $MN \times MN$  matrices, with  $\mathcal{L}$  comprising linear operators. We use the DEDALUS<sup>1</sup> project, a general-purpose spectral code (Burns et al. 2020), to solve the linear eigenvalue problem. We employ a numerical resolution of  $N = 256$ , and when necessary, increase the resolution by a factor of 1.5 to eliminate non-physical modes. By comparing solutions at different resolutions, we retain only the valid modes within a tolerance of  $10^{-6}$ .

## 4 RESULTS

We first examine the influence of magnetic fields on the RWI growth in the ideal MHD regime. Figure 1 illustrates the growth rate  $\gamma$  as a function of  $\beta$ , where a large  $\beta$  represents a weak vertical field and a small  $\beta$  indicates a strong field. When the radial field is minimal compared to the vertical component ( $|B_{r0}|/B_{z0} \leq 0.01$ ), the growth rates are similar to those of the pure  $B_z$  case presented in Paper I (their top panel; Figure 3). However, strong radial fields reduce the growth rate for small  $\beta$ . This result contrasts with Yu & Lai (2013), who found that growth rates increase with decreasing  $\beta$  for constant vertical and non-zero radial fields (see their Figures 2 and 5). The reason for this discrepancy is unclear, but differences in methodology may contribute; Yu & Lai (2013) used a relaxation method to solve Lagrangian perturbations and vertically integrated equations.

In Paper I, the pure  $B_z$  model shows little sensitivity to  $\beta$

<sup>1</sup> <https://dedalus-project.org/>

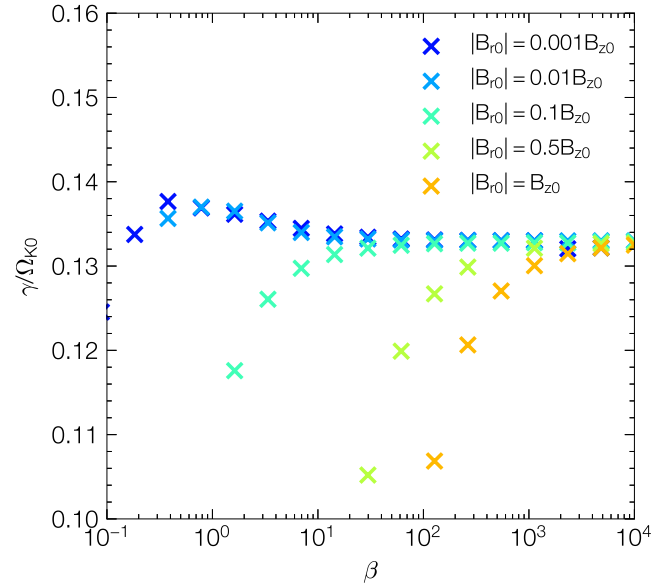
unless the fields are very strong; growth rates begin to decline when  $\beta \leq 1$ . In contrast, the pure  $B_\phi$  model indicates that growth rates already start to decrease at relatively weaker field strengths, around  $\beta \sim 100$ . Figure 1 demonstrates that the presence of a radial field contributes to the reduction of growth rates at large  $\beta$  in a  $B_z$  disk. Global 3D numerical simulations suggest that radial and vertical fields become comparable in the quasi-steady state (e.g., Gressel et al. 2020; Cui & Bai 2021, 2022). When  $|B_{r0}| \approx |B_{z0}|$ , the growth rates drop from hydrodynamic values at approximately  $\beta \sim 10^3 - 10^4$ , which are typical field strengths in protoplanetary disks.

Figure 2 depicts growth rate versus Elsasser number at a fixed  $\beta = 1$  for three non-ideal MHD effects. Filled markers represent cases with weaker radial fields, while unfilled markers denote stronger radial fields. In Paper I, we observed that in the regime of strong non-ideal MHD (small Elsasser numbers), the growth rates can closely resemble those found in hydrodynamic cases. This observation is consistent with the results for  $B_r$  shown in Figure 2. Figure 1 further illustrates that when radial fields are weak, the growth rates at  $\beta = 1$  differ only slightly from those at  $\beta = 10^4$ . For  $|B_{r0}|/B_{z0} = 0.01$ ,  $\gamma/\Omega_{K0} \approx 0.1365$  at  $\beta \approx 1.62$  and  $\gamma/\Omega_{K0} \approx 0.133$  at  $\beta = 10^4$ . As expected, the growth rates for weaker radial fields tend to plateau. For  $|B_{r0}|/B_{z0} = 0.1$ , RWI modes exhibit  $\gamma/\Omega_{K0} \approx 1.176$  at  $\beta \approx 1.62$ , showing a greater deviation from the hydrodynamic limit. At an Elsasser number of 100 and  $\beta = 1$ , the growth rates for Ohmic resistivity, Hall drift, and ambipolar diffusion are  $\gamma/\Omega_{K0} \approx 1.093, 1.059, \text{ and } 1.056$ , respectively. As the Elsasser number decreases, the growth rates for all three non-ideal MHD effects converge toward the hydrodynamic limit.

For simplicity, we set the vertical wavenumber to zero,  $k_z = 0$ , throughout the analysis. A more accurate approach would involve incorporating the vertical structure of the disk and considering background quantities as functions of disk height. However, since RWI is a radially global problem, using a vertically stratified disk model would result in 2D matrix eigenvalue problems with a matrix size that would be too large to handle. For instance, if the grid sizes in both dimensions are the same, the matrix size would be  $N^2 \times N^2$  compared to a 1D problem of size  $N \times N$ .

## 5 SUMMARY

In Paper I, we explored the influence of pure azimuthal and vertical magnetic fields on the RWI. In this study, we extend our analysis by incorporating radial magnetic fields into the background state and investigating their impact on RWI linear modes using Eulerian perturbations. Our analysis covers both the ideal MHD regime and the non-ideal MHD regime, considering effects of Ohmic resistivity, Hall drift, and ambipolar diffusion. The presence of radial field is linked to disk's vertical shear and vertical magnetic field. We employ the spectral code DEDALUS to solve the resulting matrix eigenvalue problems. Our findings indicate that radial fields exhibit behavior similar to vertical fields. In the ideal MHD limit, radial fields amplify the effect of vertical fields in reducing growth rates. This reduction in growth rates begins at relatively weak field strengths, around  $\beta \sim 10^3 - 10^4$ , which are pertinent to protoplanetary disks. In the non-ideal MHD



**Figure 1.** Growth rate versus plasma  $\beta$  for  $|B_{r0}|/B_{z0} = 0.001, 0.01, 0.1, 0.5, 1$  in the ideal MHD limit.

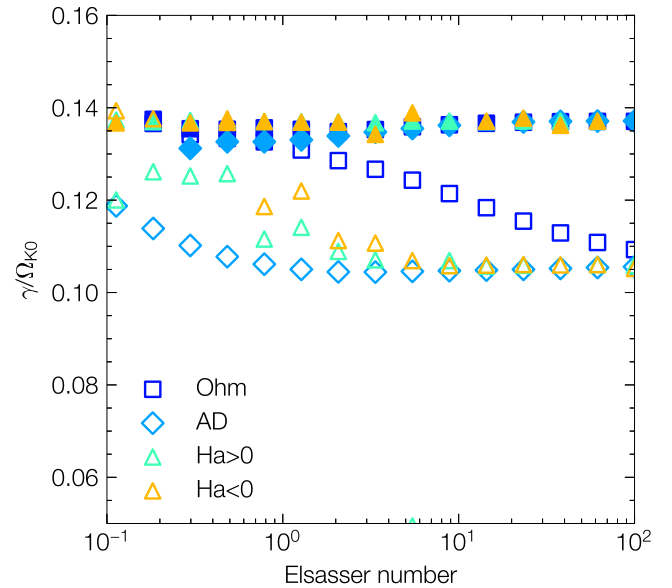


**Figure 2.** Growth rate versus Elsasser number at  $\beta = 1$  for  $|B_{r0}| = 0.01 B_{z0}$  (filled) and  $|B_{r0}| = 0.1 B_{z0}$  (unfilled) in the non-ideal MHD limit.

limit, all three non-ideal effects, when sufficiently strong, cause the growth rates to closely approximate those found in hydrodynamic models.

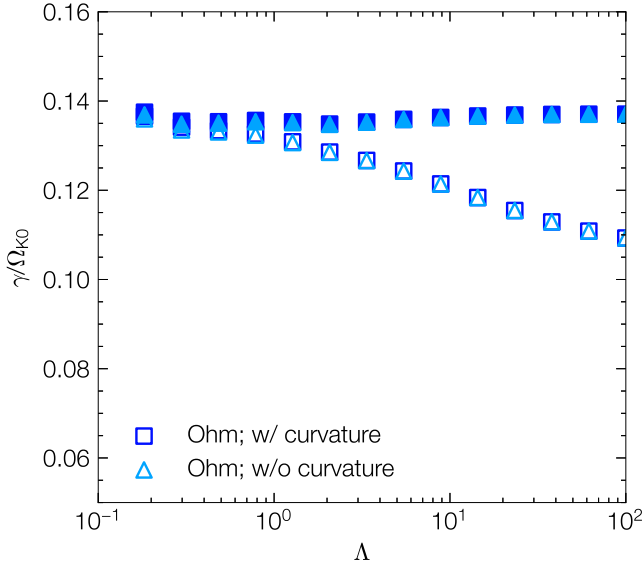


**Figure A1.** Growth rate versus Ohmic Elsasser number  $\Lambda$  at  $\beta = 1$  for  $|B_{r0}| = 0.01B_{z0}$  (filled) and  $|B_{r0}| = 0.1B_{z0}$  (unfilled) with (squares) and without (triangles) curvature terms.

## ACKNOWLEDGEMENTS

CC acknowledges funding from Natural Sciences and Engineering Research Council of Canada and UK STFC grant ST/T00049X/1.

## DATA AVAILABILITY

The data underlying this article will be shared on reasonable request to the corresponding author.

## APPENDIX A: CURVATURE TERMS IN LINEARIZED INDUCTION EQUATIONS

Figure A1 illustrates the growth rate versus Ohmic Elsasser number  $\Lambda$  for perturbed induction equations (36)–(38), both with and without curvature terms. The results show that the growth rates are largely unaffected by the inclusion of curvature terms.

## REFERENCES

- Armitage P. J., 2011, *ARA&A*, **49**, 195  
 Barker A. J., Latter H. N., 2015, *MNRAS*, **450**, 21  
 Burns K. J., Vasil G. M., Oishi J. S., Lecoanet D., Brown B. P., 2020, *Physical Review Research*, **2**, 023068  
 Chang E., Youdin A. N., 2024, *arXiv e-prints*, p. arXiv:2407.12722  
 Chang E., Youdin A. N., Krapp L., 2023, *ApJ*, **946**, L1  
 Cimerman N. P., Rafikov R. R., 2023, *MNRAS*, **519**, 208  
 Cui C., Bai X.-N., 2021, *MNRAS*, **507**, 1106  
 Cui C., Bai X.-N., 2022, *MNRAS*, **516**, 4660  
 Cui C., Tripathi A., Yu C., Lin M.-K., Youdin A., 2024, *arXiv e-prints*, p. arXiv:2407.02103  
 Galli D., Shu F. H., 1993, *ApJ*, **417**, 220  
 Girart J. M., Rao R., Marrone D. P., 2006, *Science*, **313**, 812

- Girart J. M., Beltrán M. T., Zhang Q., Rao R., Estalella R., 2009, *Science*, **324**, 1408  
 Godon P., Livio M., 1999, *ApJ*, **523**, 350  
 Goldreich P., Tremaine S., 1979, *ApJ*, **233**, 857  
 Goldreich P., Ward W. R., 1973, *ApJ*, **183**, 1051  
 Gressel O., Ramsey J. P., Brinch C., Nelson R. P., Turner N. J., Bruderer S., 2020, *ApJ*, **896**, 126  
 Güttler C., Blum J., Zsom A., Ormel C. W., Dullemond C. P., 2010, *A&A*, **513**, A56  
 Hammer M., Kratter K. M., Lin M.-K., 2017, *MNRAS*, **466**, 3533  
 Hsu C.-Y., Li Z.-Y., Tu Y., Hu X., Lin M.-K., 2024, *arXiv e-prints*, p. arXiv:2407.08032  
 Huang J., et al., 2018, *ApJ*, **869**, L42  
 Latter H. N., Papaloizou J., 2018, *MNRAS*, **474**, 3110  
 Lesur G., 2021, *Journal of Plasma Physics*, **87**, 205870101  
 Li H., Finn J. M., Lovelace R. V. E., Colgate S. A., 2000, *ApJ*, **533**, 1023  
 Li H., Colgate S. A., Wendroff B., Liska R., 2001, *ApJ*, **551**, 874  
 Li Y.-P., Li H., Li S., Birnstiel T., Drażkowska J., Stammler S., 2020, *ApJ*, **892**, L19  
 Lin C. C., Shu F. H., 1964, *ApJ*, **140**, 646  
 Lovelace R. V. E., Li H., Colgate S. A., Nelson A. F., 1999, *ApJ*, **513**, 805  
 Lyra W., Mac Low M.-M., 2012, *ApJ*, **756**, 62  
 Meheut H., Keppens R., Casse F., Benz W., 2012, *A&A*, **542**, A9  
 Miranda R., Lai D., Méheut H., 2016, *MNRAS*, **457**, 1944  
 Miranda R., Li H., Li S., Jin S., 2017, *ApJ*, **835**, 118  
 Tassoul J.-L., 1978, *Theory of rotating stars*  
 Tsang D., Lai D., 2008, *MNRAS*, **387**, 446  
 Wang L., Bai X.-N., Goodman J., 2019, *ApJ*, **874**, 90  
 Wardle M., Ng C., 1999, *MNRAS*, **303**, 239  
 Weidenschilling S. J., 1977, *Ap&SS*, **51**, 153  
 Weidenschilling S. J., Cuzzi J. N., 1993, in Levy E. H., Lunine J. I., eds, *Protostars and Planets III*. p. 1031  
 Youdin A. N., Goodman J., 2005, *ApJ*, **620**, 459  
 Yu C., Lai D., 2013, *MNRAS*, **429**, 2748  
 Zhu Z., Stone J. M., 2014, *ApJ*, **795**, 53  
 Zhu Z., Stone J. M., Rafikov R. R., Bai X.-n., 2014, *ApJ*, **785**, 122  
 Zsom A., Ormel C. W., Güttler C., Blum J., Dullemond C. P., 2010, *A&A*, **513**, A57  
 van der Marel N., et al., 2021, *AJ*, **161**, 33

This paper has been typeset from a  $\text{\TeX}/\text{\LaTeX}$  file prepared by the author.